

# Experimental implementation of an emission-aware prosumer with online flexibility quantification and provision

Hanmin Cai<sup>\*</sup>, Philipp Heer

Urban Energy System Lab, Empa, Überlandstrasse 129, 8600 Dübendorf, Switzerland

## ARTICLE INFO

### Keywords:

Flexibility envelope  
Demand side management  
Model predictive control  
Emission-aware  
Prosumer

## ABSTRACT

Active building energy management can facilitate the development of low-carbon buildings and support flexible operations of future smart cities, thanks to advancements in digitalization. To fully leverage these benefits, it is essential to integrate diverse objectives and engage multiple stakeholders. However, a gap remains in comprehensive field insights into emission reduction, flexibility provision, and user impacts. This study examined how a real occupied building, with all its energy assets, could function as an emission-aware prosumer with flexible energy consumption. An existing building energy management system was enhanced by integrating a model predictive control strategy. The setup reduced equivalent carbon emissions from electricity imports and provided flexibility to the energy system. The experimental results indicate an emission reduction of 12.5% compared to a rule-based controller that maximized PV self-consumption. In addition, a minimal flexibility provision experiment was demonstrated with a locally emulated distribution system operator. The results suggest that flexibility was provided without the risk of rebound effects, as flexibility was quantified and communicated to the system operator in advance. This study demonstrates the feasibility of low-carbon buildings and their support for flexible energy systems, while also identifying and discussing practical scalability challenges.

## 1. Introduction

As the share of intermittent Renewable Energy Sources (RES) increases and conventional power plants are being phased out, there is an increasing need for flexible demand to support system operation (Ostergaard et al., 2021). Meanwhile, buildings account for 28% of the global energy-related CO<sub>2</sub> emissions attributed to their operations (Global Alliance for Buildings and Construction & International Energy Agency and United Nations Environment Programme, 2020). As the level of digitalization in the building sector increases, Demand Side Management (DSM) can facilitate low-carbon operations and make buildings integral parts of the energy infrastructure, supporting cities in their transition towards net-zero targets (Vigna, Pernetti, Pasut, & Lollini, 2018). A recent study (Gupta et al., 2021) indicates that utilizing demand-side flexibility presents significant economic opportunities to facilitate the transition toward a sustainable future. A comprehensive understanding at the building level is crucial for the practical mass rollout, an area that is currently underdeveloped, as discussed in Ref. Le Déau et al. (2023).

This new role for buildings introduces diverse objectives and involves a variety of stakeholders (Jensen et al., 2017). Realistic DSM

strategies are increasingly needed to consider multiple aspects, namely emission reduction, flexibility quantification and provision (Li et al., 2022). Additionally, occupants' thermal comfort and preferences need to be respected. In fact, the bottom-up nature of building energy flexibility utilization places occupants in the central stage (Nagy et al., 2023). However, many existing studies examine the topic with limited types of flexibility resources, concentrate solely on simulation studies and address just one of the mentioned aspects. Li, Wang, Hong, and Piette (2021) provide a review of energy flexibility in residential buildings and highlight the existing gap in the comprehensive consideration of all available resources. Additionally, the lack of clear requirements and credits for the provision of flexibility is identified.

Several existing studies focus on examining limited aspects of the mentioned gap. Refs. Bolzoni, Parisio, Todd, and Forsyth (2021) and Péan, Costa-Castelló, and Salom (2019) develop Model Predictive Control (MPC) strategies to manage flexible assets, reporting considerable emission and cost reductions. Although their works partially include experimental testing, most control targets are emulated using a Real-Time Digital Simulator (RTDS). Such emulation omits potential disturbances from occupants, which can impact emission reduction and flexibility potentials. Moreover, the impacts of flexibility utilization on users'

<sup>\*</sup> Corresponding author.

E-mail address: [hanmin.cai@empa.ch](mailto:hanmin.cai@empa.ch) (H. Cai).

Nomenclature	
COP	Coefficient of Performance
DHW	Domestic Hot Water
DSM	Demand Side Management
DSO	Distribution System Operator
EV	Electric Vehicle
HVAC	Heating, Ventilation and Air Conditioning
HP	Heat Pump
MPC	Model Predictive Control
OCP	Optimal Control Problem
PV	Photovoltaic
RES	Renewable Energy Resources
SH	Space Heating
SOC	State of Charge

thermal comfort levels cannot be verified. Nonetheless, these works demonstrate MPC's capability of handling complex tasks. Pergantis et al. (2024) provide a comprehensive review of all known field demonstrations of supervisory control for residential HVAC, noting that only one field study explicitly incorporates emissions within the objectives of predictive control (Thorsteinsson et al., 2023). Following this discussion on predictive control, Heinrich, Ziras, Syrris, and Bindner (2020) provide a retrospective analysis of the flexibility provision in an island-scale experiment, where flexibility is delivered in an open-loop fashion. In addition, Munankarmi, Jin, Ding, and Zhao (2020) examine the flexibility of all behind-the-meter resources of a residential building. This flexibility is further quantified to facilitate interactions between buildings and Distribution System Operators (DSOs). However, the study relies on perfect knowledge of baseline power and rebound effects have been observed. De Coninck and Helsen (2016) propose to represent flexibility with a cost curve, comprising sub-optimality gaps due to set-point tracking. Maasoumy, Rosenberg, Sangiovanni-Vincentelli, and Callaway (2014) propose a scheme that allows utilities to contract buildings for power flexibility provision, and feasible power levels are calculated accounting for operational limits. Although an experiment is reported, its main purpose is to verify that the high-frequency components of utility's flexibility signal can be tracked. Additionally, both De Coninck and Helsen (2016) and Maasoumy et al. (2014) assume that flexibility provision duration is known a priori.

This study focuses on self-reported flexibility, characterized as the capability of modifying energy usage patterns without violating appliance operation limits or compromising end-user preferences and thermal comfort. To this end, the flexibility envelope concept presented in Gasser, Cai, Karagiannopoulos, Heer, and Hug (2021) is adopted. It captures time dependency, the impacts of anticipated weather conditions, and end users' energy usage patterns without assuming knowledge of flexibility provision duration. Compared to traditional ripple control (Westermann & John, 2007), flexibility envelope offers a significant advantage. It allows DSOs to obtain a comprehensive overview of available flexibility, effectively combining all flexibility resources. The high-resolution flexibility supports precisely resolve potential network issues. From this perspective, the flexibility quantification in De Coninck and Helsen (2016) and Maasoumy et al. (2014) can be seen as special cases of the flexibility envelope. However, Gasser et al. (2021) only analyzes flexibility quantification in an open-loop fashion and in a pure simulation-based environment. Comparison of relevant research works is summarized in Table 1

Based on the papers reviewed, there remains a gap in comprehensive experimental insights covering three aspects: (1) emission-aware operation, (2) flexibility quantification and provision to DSO, and (3) the impacts on and from occupants. A thorough investigation of these aspects is essential for the successful deployment of flexible buildings at a cluster scale (Azizi, Ahmadihangar, Rosin, & Bolouki, 2022). The main contributions of this paper are threefold. Firstly, we present an

emission-aware MPC as the base strategy for a prosumer. The emission reduction and occupants' thermal comfort levels are quantified in real-life operations. Secondly, online flexibility quantification and provision are formulated as optimization problems that can be automated to ease the practical deployment. The framework is experimentally demonstrated with an emulated DSO and the risk of rebound effects is assessed. Lastly, qualitative and quantitative insights into impacts on and from occupants are reported. While ensuring thermal comfort is incorporated into the control strategy, impacts from occupants are assessed in an ex-post analysis.

The remainder of the paper is organized as follows: Section 2 presents the methodological framework of controller design, flexibility quantification and provision. Section 3 describes the experimental setup and Section 4 presents the results of a week-long experiment, the real-world implications of which are critically discussed in Section 5. Finally, Section 6 gives a brief summary and identifies areas for further research.

## 2. Methodology

This section first presents control-oriented models and operating constraints of all the assets, followed by describing the parameter identification process. Then, the Optimal Control Problem (OCP) formulation of the MPC controller is provided using the obtained models. Following this, the flexibility envelope calculation and an interaction scheme between the building and the DSO are unified with the mentioned MPC in one mathematical framework.

### 2.1. Control-oriented model structures for experiments

The considered behind-the-meter assets include Heat Pumps (HPs) for Space Heating (SH) and Domestic Hot Water (DHW), a stationary battery, an Electric Vehicle (EV) with bidirectional charging, uncontrolled loads and a rooftop Photovoltaics (PV) installation. The model structures are chosen based on a trade-off among computational complexity, required measurements and interpretability.

Throughout the paper, we use  $\hat{\cdot}$  to denote forecast values and use  $t$  as the time index. We focus on controlling the active power of behind-the-meter assets while neglecting the reactive power that is in general not available to control for residential loads. Power consumption is treated as positive, leading to PV power output and battery/EV discharging power being negative. Lastly, we use  $\mathbb{R}_+$  and  $\mathbb{R}_-$  to refer to the set of non-negative and non-positive real values respectively.

#### 2.1.1. Space heating

Although non-linearity exists, when the room temperature in buildings is actively controlled within a limited range, the dynamics of each zone can be approximated with an affine model for closed-loop control. Preliminary experimental studies also show that high-order

Table 1

Comparison of relevant research works.

Ref.	Emission-aware	Flexibility quant.	Flexibility prov.	Occupants	Experiment
Bolzoni et al. (2021)	✓	✗	✗	✗	✓
Péan et al. (2019)	✓	✓	✗	✗	✗
Thorsteinsson et al. (2023)	✓	✗	✗	✓	✓
Heinrich et al. (2020)	✗	✓	✓	✗	✓
Munankarmi et al. (2020)	✗	✓	✓	✗	✗
De Coninck and Helsén (2016)	✗	✓	✗	✗	✗
Maasoumy et al. (2014)	✗	✓	✓	✓	✓
Gasser et al. (2021)	✓	✓	✓	✗	✗
Westermann and John (2007)	✗	✗	✓	✗	✗
This work	✓	✓	✓	✓	✓

models tend to perform worse than low-order models (Decoussemaeker, 2020). The current study considers each room as one zone, with the indoor temperature given by:

$$T_{i,t+1}^{\text{sh}} = A^{\text{sh}} T_{i,t}^{\text{sh}} + B^{\text{sh}} \phi_{i,t}^{\text{sh}} + E^{\text{sh}} \begin{bmatrix} \hat{T}_t^{\text{amb}} \\ \hat{\phi}_t^{\text{irr}} \end{bmatrix}, \quad \forall t \in H, \quad \forall i \in I, \quad (1)$$

where  $T_{i,t}^{\text{sh}}$  is the room temperature,  $\phi_{i,t}^{\text{sh}}$  is the thermal power input,  $\hat{T}_t^{\text{amb}}$ ,  $\hat{\phi}_t^{\text{irr}}$  are the ambient temperature and the solar irradiance forecast respectively,  $H$  is the time horizon,  $i$  is the room index and  $I$  is the set of rooms. Since only weather forecast is available in real-time control,  $\hat{T}_t^{\text{amb}}$  and  $\hat{\phi}_t^{\text{irr}}$  are used directly. Internal heat gain is omitted as a disturbance term in this control-oriented model, primarily due to the absence of occupancy detection devices and the unreliability of zone-level forecasts in practice. In addition, we consider continuous thermal power to the rooms and the equivalent thermal power output can be obtained by modulating an HP operating in an ON/OFF mode with a pulse width modulation strategy. The corresponding electrical power consumption of the HP is given by:

$$P_t^{\text{sh}} = \sum_{i \in I} \phi_{i,t}^{\text{sh}} / \text{COP}^{\text{m}}, \quad \forall t \in H, \quad (2)$$

where  $\text{COP}^{\text{m}}$  denotes the COP of the HP for SH. The corresponding constraints are given by:

$$T_{i,t}^{\text{sh},\min} - \epsilon_{i,t}^{\text{sh}-} \leq T_{i,t}^{\text{sh}} \leq T_{i,t}^{\text{sh},\max} + \epsilon_{i,t}^{\text{sh}+}, \quad \forall t \in H, \quad \forall i \in I, \quad (3)$$

$$\epsilon_{i,t}^{\text{sh}-} \geq 0, \quad \epsilon_{i,t}^{\text{sh}+} \geq 0, \quad \forall t \in H, \quad \forall i \in I, \quad (4)$$

$$0 \leq P_t^{\text{sh}} \leq P^{\text{sh},\max}, \quad \forall t \in H, \quad (5)$$

where  $T_{i,t}^{\text{sh},\max}$  and  $T_{i,t}^{\text{sh},\min}$  are the predefined time-varying upper and lower indoor temperature limits respectively,  $\epsilon_{i,t}^{\text{sh}-}$  and  $\epsilon_{i,t}^{\text{sh}+}$  are the slack variables introducing soft constraints to ensure feasible solutions, and  $P^{\text{sh},\max}$  is the electrical power capacity of the HP.

### 2.1.2. Domestic hot water heating

DHW is supplied by a fixed-speed HP operating on ON/OFF mode with a buffer tank. Stratification effects within the tank are neglected, and the average tank temperature is given by:

$$T_{t+1}^{\text{dhw,avg}} = A^{\text{dhw}} T_t^{\text{dhw,avg}} + B^{\text{dhw}} \phi_t^{\text{dhw}} + E^{\text{dhw}} m_t^{\text{draw}}, \quad \forall t \in H, \quad (6)$$

where  $T_t^{\text{dhw,avg}}$  is the volume-weighted average tank temperature,  $\phi_t^{\text{dhw}}$  is the thermal power input and  $m_t^{\text{draw}}$  is the amount of water draw. The corresponding electrical power consumption of the HP can be given by:

$$P_t^{\text{dhw}} = \phi_t^{\text{dhw}} / \text{COP}^{\text{h}}, \quad \forall t \in H, \quad (7)$$

where  $\text{COP}^{\text{h}}$  is used to differentiate from the above-mentioned SH HP. This distinction is made because SH and DHW typically have different inlet temperatures. Average tank temperature constraints are given by:

$$T_t^{\text{dhw},\min} - \epsilon_t^{\text{dhw}-} \leq T_t^{\text{dhw}} \leq T_t^{\text{dhw},\max} + \epsilon_t^{\text{dhw}+}, \quad \forall t \in H, \quad (8)$$

$$\epsilon_t^{\text{dhw}-} \geq 0, \quad \epsilon_t^{\text{dhw}+} \geq 0, \quad \forall t \in H, \quad (9)$$

where  $T_t^{\text{dhw},\max}$  and  $T_t^{\text{dhw},\min}$  are the predefined time-varying upper and lower average tank temperature limits respectively,  $\epsilon_t^{\text{dhw}-}$  and  $\epsilon_t^{\text{dhw}+}$  are the slack variables enforcing soft constraints. The ON/OFF operating mode is modeled with a binary variable  $z_t^{\text{dhw}}$ :

$$P_t^{\text{dhw}} = P^{\text{dhw},\max} z_t^{\text{dhw}}, \quad \forall t \in H, \quad (10)$$

where  $P^{\text{dhw},\max}$  is the electric power capacity of the DHW HPs.

### 2.1.3. Stationary electric battery

A model that captures battery self-losses, charging/discharging efficiencies is given by:

$$\text{SOC}_{t+1}^{\text{ebat}} = A^{\text{ebat}} \text{SOC}_t^{\text{ebat}} + B^{\text{ebat}} \begin{bmatrix} P_t^{\text{ebat, ds}} \\ P_t^{\text{ebat, ch}} \end{bmatrix}, \quad \forall t \in H, \quad (11)$$

where  $\text{SOC}_t^{\text{ebat}}$  is the battery State-Of-Charge (SOC),  $P_t^{\text{ebat, ch}} \in \mathbb{R}_+$  and  $P_t^{\text{ebat, ds}} \in \mathbb{R}_-$  are the battery charging and discharging power respectively. The mutual exclusiveness of  $P_t^{\text{ebat, ch}}$  and  $P_t^{\text{ebat, ds}}$  is enforced with a binary variable  $z_t^{\text{ebat}}$  as follows.

$$0 \leq P_t^{\text{ebat, ch}} \leq P^{\text{ebat},\max} z_t^{\text{ebat}}, \quad \forall t \in H, \quad (12)$$

$$-P^{\text{ebat},\max}(1 - z_t^{\text{ebat}}) \leq P_t^{\text{ebat, ds}} \leq 0, \quad \forall t \in H, \quad (13)$$

$$\text{SOC}^{\text{ebat},\min} - \epsilon_t^{\text{ebat}} \leq \text{SOC}_t^{\text{ebat}} \leq 100, \quad \forall t \in H, \quad (14)$$

$$\epsilon_t^{\text{ebat}} \geq 0, \quad \forall t \in H, \quad (15)$$

where  $\epsilon_t^{\text{ebat}}$  is the slack variables introducing soft constraints to ensure feasible solutions and  $\text{SOC}^{\text{ebat},\min}$  is the minimum SOC.

### 2.1.4. Electric vehicle

Similar to the stationary battery model, the EV battery is modeled as follows:

$$\text{SOC}_{t+1}^{\text{ev}} = A^{\text{ev}} \text{SOC}_t^{\text{ev}} + B^{\text{ev}} \begin{bmatrix} P_t^{\text{ev, ds}} \\ P_t^{\text{ev, ch}} \end{bmatrix}, \quad \forall t \in H, \quad (16)$$

where  $\text{SOC}_t^{\text{ev}}$  is the EV battery SOC,  $P_t^{\text{ev, ch}} \in \mathbb{R}_+$  and  $P_t^{\text{ev, ds}} \in \mathbb{R}_-$  are the battery charging and discharging power respectively. The limits on SOC is given by:

$$\text{SOC}^{\text{ev},\min} - \epsilon_t^{\text{ev}} \leq \text{SOC}_t^{\text{ev}} \leq 100, \quad \forall t \in H, \quad (17)$$

$$\epsilon_t^{\text{ev}} \geq 0, \quad \forall t \in H, \quad (18)$$

where  $\epsilon_t^{\text{ev}}$  is the slack variable introducing soft constraints and  $\text{SOC}^{\text{ev},\min}$  is the minimum SOC of EV battery. Simultaneous charging/discharging are avoided by introducing a binary variable  $z_t^{\text{ev}}$  as follows.

$$0 \leq P_t^{\text{ev, ch}} \leq P^{\text{ev},\max} z_t^{\text{ev}}, \quad \forall t \in H, \quad (19)$$

$$-P_t^{\text{ev,max}}(1 - z_t^{\text{ev}}) \leq P_t^{\text{ev, ds}} \leq 0, \forall t \in C, \quad (20)$$

$$P_t^{\text{ev, ch}} = 0, P_t^{\text{ev, ds}} = 0, \forall t \in H \setminus C, \quad (21)$$

$$\text{SOC}_{\sup C}^{\text{ev,min}} \leq \text{SOC}_{\sup C}^{\text{ev}} \leq 100, \quad (22)$$

where  $C$  is the set of time steps when the EV is connected to the charger at home. Constraint (21) indicates EV is not available for control when absent and zero power exchange is assumed. Constraint (22) ensures minimum departure state-of-charge  $\text{SOC}_{\sup C}^{\text{ev,min}}$  with  $\sup C$  being the departure time instant or the supremum of the set  $C$ .

### 2.1.5. Photovoltaic

PV power output is predicted based on weather forecast and the formulation is given by:

$$\hat{P}_t^{\text{pv}} = \beta_0^{\text{pv}} + \beta_1^{\text{pv}} \hat{\phi}_t^{\text{irrd}} + \beta_2^{\text{pv}} \hat{T}_t^{\text{amb}} + \epsilon, \quad (23)$$

where  $\hat{P}_t^{\text{pv}} \in \mathbb{R}_+$  is the predicted PV output. Such numerical weather condition-based forecasting is effective for horizons exceeding 4 h (Ahmed, Sreeram, Mishra, & Arif, 2020), whereas persistence forecast is popular for short-term PV forecasting. Hence, PV power forecast  $\{\hat{P}_t^{\text{pv}} | t \in H\}$  within the prediction horizon  $H$  is additionally combined with a persistence forecast. Since PV output forecasting is not the focus of this work, the combination of both forecast is determined empirically. The result is used in the predictive controller. Coefficients  $(\beta_0^{\text{pv}}, \beta_1^{\text{pv}}, \beta_2^{\text{pv}})$  are re-identified every day accounting for the impact of potential coverings on the installation, such as leaves and snow. The coefficients are updated if the re-identification is satisfactory.

### 2.1.6. Uncontrolled loads

Uncontrolled loads refer to lighting, cooking and wet appliances. This study aggregates the power  $\hat{P}_t^{\text{fix}} \in \mathbb{R}_+$  of these appliances to account for their electricity consumption. The forecast is a combination of a 15-min ahead persistence forecast and a 24-h ahead persistence forecast.

### 2.1.7. Entire building

The energy balance of the entire building is given by:

$$P_t^{\text{btg}} + P_t^{\text{gtb}} = P_t^{\text{sh}} + P_t^{\text{dhw}} + P_t^{\text{ebat,ch}} + P_t^{\text{ebat,ds}} + P_t^{\text{ev,ch}} + P_t^{\text{ev,ds}} + \hat{P}_t^{\text{pv}} + \hat{P}_t^{\text{fix}}, \forall t \in H, \quad (24)$$

where  $P_t^{\text{btg}} \in \mathbb{R}_-$  and  $P_t^{\text{gtb}} \in \mathbb{R}_+$  are the electricity export and import respectively. They are differentiated because the total equivalent carbon emission is calculated according to the carbon intensity of electricity imported from the grid, and it is assumed that electricity export does not offset building's carbon footprint. To ensure the mutual exclusiveness of  $P_t^{\text{btg}}$  and  $P_t^{\text{gtb}}$ , a binary variable  $z_t^{\text{grid}}$  is introduced.

$$0 \leq P_t^{\text{gtb}} \leq M z_t^{\text{grid}}, \forall t \in H, \quad (25)$$

$$-M(1 - z_t^{\text{grid}}) \leq P_t^{\text{btg}} \leq 0, \forall t \in H, \quad (26)$$

where  $M \in \mathbb{R}_+$  is a sufficiently large constant.

## 2.2. Parameter identification

A prediction error method is used, which can be described as minimizing the differences between the observed outputs and the predicted outputs based on the model and the historical data (Ljung, 1998). For conciseness, a formulation is given as follows:

$$y_t = \hat{A}y_{t-1} + \hat{B}u_{t-1} + \epsilon_t, \quad (27)$$

where  $\hat{A}$ ,  $\hat{B}$  denote the system dynamics-related parameters that need to be identified. Eq. (27) assumes a state-space representation with

an identity matrix as its output matrix and a zero matrix as its feed-through matrix. The  $k$ -step ahead prediction based on the historical data and the model structure is formulated as follows:

$$\hat{y}_t = \hat{A}^k y_{t-k} + \sum_{i=1}^k \hat{A}^{k-i} \hat{B} u_{t-k-1+i}, \quad (28)$$

where  $\hat{y}_t$  is the  $k$ -step ahead prediction based on the historical inputs and the boundary conditions described by the set  $\{u_t | t \in [t-k, t]\}$ . The unknown parameters are obtained by optimizing the cost function consisting of accumulated prediction errors as follows:

$$J = \sum_{i=1}^N \frac{1}{N} L_\delta(\hat{y}_i, y_i), \quad (29)$$

where  $N$  denotes the number of prediction error terms and  $y_t$  is the observed output. Notably, the Huber function  $L_\delta(\cdot)$  to compute losses instead of a square function to reduce the impacts of outliers. The optimal parameters  $\hat{A}^*$  and  $\hat{B}^*$  minimizes the cost  $J$ . For this study, a prediction horizon of 24 h is chosen.

## 2.3. Optimal control problem formulation

The full OCP formulation of the MPC is given by:

$$\begin{aligned} & \text{minimize} && \sum_{t \in H} c_t^{\text{emi}} P_t^{\text{gtb}} \Delta \tau_t + L_t \Delta \tau_t, \\ & \{\mathbf{X}_t, \mathbf{U}_t, \mathbf{V}_t | \forall t \in H\} \end{aligned} \quad (30a)$$

$$\text{subject to} \quad \text{Eqs. (1) to (26)}, \quad (30b)$$

where  $L_t := w_1(L_\delta(\epsilon_t^{\text{sh}+}) + L_\delta(\epsilon_t^{\text{dhw}+})) + w_2(L_\delta(\epsilon_t^{\text{sh}-}) + L_\delta(\epsilon_t^{\text{dhw}-})) + w_3((\epsilon_t^{\text{ev}})^2 + (\epsilon_t^{\text{ebat}})^2)$  denotes the cost associated with soft constraints, Huber function  $L_\delta(\cdot)$  is used to formulate the penalties of constraint violations instead of quadratic penalties to be robust to outliers.  $w_1$ ,  $w_2$  and  $w_3$  are the customized weighting factors,  $\{\mathbf{X}_t | \forall t \in H\} := \{T_{i,t}^{\text{sh}}, T_{i,t}^{\text{dhw}}, \text{SOC}_t^{\text{ev}}, \text{SOC}_t^{\text{ebat}} | \forall t \in H, \forall i \in I\}$  is the set of state variables,  $\{\mathbf{U}_t | \forall t \in H\} := \{P_t^{\text{sh}}, P_t^{\text{dhw}}, P_t^{\text{ebat,ch}}, P_t^{\text{ebat,ds}}, P_t^{\text{ev,ch}}, P_t^{\text{ev,ds}} | \forall t \in H\}$  is the set of control input variables,  $\{\mathbf{V}_t | \forall t \in H\} := \{\epsilon_t^{\text{sh}-}, \epsilon_t^{\text{sh}+}, \epsilon_t^{\text{dhw}-}, \epsilon_t^{\text{dhw}+}, \epsilon_t^{\text{ev}}, \epsilon_t^{\text{ebat}}, z_t^{\text{ev}}, z_t^{\text{grid}}, z_t^{\text{dhw}}, P_t^{\text{btg}}, P_t^{\text{gtb}} | \forall t \in H, \forall i \in I\}$  denotes the set of the remaining decision variables,  $c_t^{\text{emi}} \in \mathbb{R}_+$  is the grid carbon intensity. It needs to be mentioned that only the variables in  $\{\mathbf{U}_t | \forall t \in H\}$  can be physically controlled. Although the rest of the variables are formulated as decision variables of the OCP, they can be determined by  $\{\mathbf{U}_t | \forall t \in H\}$ , system dynamics equations, and algebraic constraints.

In addition, a set of inequidistant sampling time intervals are used to reduce the number of decision variables as shown in Fig. 1. Larger sampling times are assumed for the time instants further in the optimization horizon, as forecast and modeling errors increase as well. The horizon is chosen to be 24 h to include future knowledge such as PV power output and EV usage patterns.

## 2.4. Flexibility envelope

The flexibility envelope<sup>1</sup>, introduced qualitatively in a previous study (Gasser et al., 2021), is formulated as optimization problems and extended to consider the flexibility from batteries, EVs with bidirectional charging, and curtailable PV.

The flexibility envelope identification starts with identifying the energy bounds by energizing flexible appliances to their extremes. The upper energy bound is identified by maximizing device consumption as early as possible, coupled with full PV output curtailment. To identify the lower energy bound, all the loads are set to consume as late and as little as possible. Simultaneously, the stationary and EV batteries are set to discharge as early and as much as possible without curtailment of PV output. The upper and lower energy bounds are illustrated as the

<sup>1</sup> An example code is provided at <https://github.com/hacai44/GRIP>.



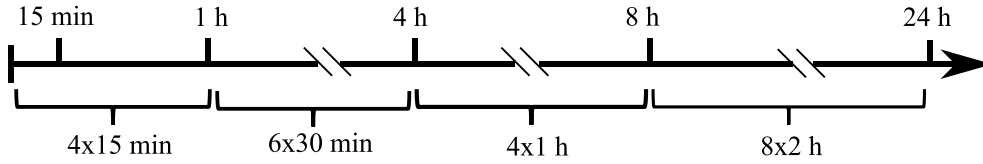


Fig. 1. Inequidistant sampling time  $\Delta t$  over an optimization horizon of 24 hours.

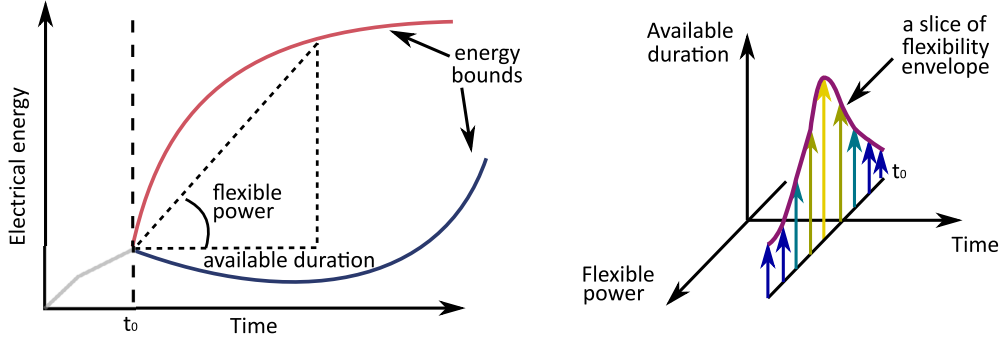


Fig. 2. Illustration of the workflow to obtain one slice of a flexibility envelope at  $t_0$ . The left figure depicts upper and lower energy bounds derived from extreme scenarios. The bounds indicate flexible power and the corresponding available duration. The right figure maps the power levels and duration onto a three-dimensional space and illustrates one slice of flexibility envelope. All slices at each time step within the horizon constitute a full flexibility envelope.

red and blue curves in Fig. 2. Formally, the above-mentioned notion can be formulated as optimization problems by modifying the OCP formulation in Eq. (30). Initially, solving the original OCP gives  $\{\bar{X}_t, \bar{U}_t, \bar{V}_t | t \in H\}$ , in which  $\{\bar{X}_t | t \in H\}$  are the optimal state trajectories. The cost functions for deriving the upper and the lower energy bounds are defined as  $J^\uparrow := \sum_{t \in H} L_t - e^{-\frac{t}{\delta}} U_t$  and  $J^\downarrow := \sum_{t \in H} L_t + e^{-\frac{t}{\delta}} U_t$  respectively, in which  $e^{-\frac{t}{\delta}}$  is an exponentially decaying weighting factor. Moreover, these optimization problems are initialized using the optimal state trajectories  $\bar{X}_t$ . Solving the OCP with the new cost functions, we have  $\{U_t^\uparrow | t \in H'\} = \text{argmin}_{\{X_t, U_t, V_t | t \in H'\}} J^\uparrow$  and  $\{U_t^\downarrow | t \in H'\} = \text{argmin}_{\{X_t, U_t, V_t | t \in H'\}} J^\downarrow$ , in which  $H'$  is the optimization horizon for energy bounds identification and it might be different from  $H$ . Denote the aggregate power of all assets except uncontrolled loads as  $P_t \in \mathbb{R}$  and we further have  $P_t^\uparrow$  and  $P_t^\downarrow$  as the aggregated power calculated from  $U_t^\uparrow$  and  $U_t^\downarrow$  respectively. With  $\{P_t^\uparrow, P_t^\downarrow | t \in H'\}$ , the upper and lower energy bounds can be obtained as  $\{E_n^\uparrow := \sum_{k=1}^n P_k^\uparrow \Delta \tau_k | \forall n \in H'\}$  and  $\{E_n^\downarrow := \sum_{k=1}^n P_k^\downarrow \Delta \tau_k | \forall n \in H'\}$ . The energy bounds of the PV installation are calculated differently as there is no inter-temporal correlation. For a curtailable PV, the upper and the lower energy bounds are given by  $\{E_n^\uparrow := 0 | \forall n \in H'\}$  and  $\{E_n^\downarrow := \sum_{k=1}^n \hat{P}_k^{\text{PV}} \Delta \tau_k | \forall n \in H'\}$  respectively. Finally, we can obtain the energy bounds of the entire building by combining the above-mentioned bounds. To ease the computational efforts, power of all assets is approximated as continuous variables, at the expense of introducing biases.

In essence, system dynamics and operational limits determine the energy bounds, which encompass all feasible energy trajectories.  $\{P_k | E_n^\downarrow \leq \sum_{k=1}^n P_k \Delta \tau_k \leq E_n^\uparrow, n \in H', k \in H'\}$ , which is an infinite set due to continuously controllable set points of the components. To ease representation, we consider only power trajectories with invariant power levels as the dashed line in Fig. 2 shows with the slope indicating the power. The corresponding available duration is limited by the second endpoint of the line. Denote a future time instant as  $\tau \in \mathcal{T}_+$  and feasible power level as  $P \in \mathcal{P}_\tau$ . The mentioned available duration is represented as an implicit function of power level and time  $f: \mathbb{R} \times \mathcal{T}_+ \rightarrow \mathbb{R}_+$ . To summarize, the flexibility envelope is a three-dimensional surface, comprised of points in the set  $\{(\tau, P, f(\tau, P)) | \tau \in \mathcal{T}_+, P \in \mathcal{P}_\tau\}$ . Since the flexibility envelope captures energetic flexibility, the available duration and the flexible power level exhibit an inversely proportional relationship.

## 2.5. Interaction between buildings and a DSO

The proposed flexibility envelope captures the thermal inertia of a building, the storage of a domestic hot water tank, the bidirectional charging of a stationary electric battery and/or an EV, and the curtailable PV power. When this envelope is communicated in advance, a DSO obtains a comprehensive overview of the available flexibility at a given building. Upon receiving the flexibility envelope, the DSO sends a flexibility provision message  $(\tau_s, \tau_e, P)$  to the building, where  $\tau_s$  and  $\tau_e$  denote the starting time and the ending time of flexibility provision respectively, and  $P \in \mathcal{P}_\tau$  denotes the power level that needs to be tracked. By definition, there is  $\tau_e - \tau_s \leq f(\tau, P)$ . Upon receiving  $(\tau_s, \tau_e, P)$ , the cost function of the OCP is extended. It now includes the cost of tracking errors with the weighting factor  $\omega_4$  and the resultant is  $J := \sum_{t \in H} c_t^{\text{emi}} P_t^{\text{gtb}} \Delta \tau_t + L_t \Delta \tau_t + \omega_4 (P_t^{\text{gtb}} + P_t^{\text{btg}} - \hat{P}_t^{\text{fix}} - P)^2 \Delta \tau_t$ .

Moreover, the overall two-stage framework is illustrated in Fig. 3. This framework allows the DSO to address local network issues using local flexibility resources. When there is a sufficient number of buildings supporting this framework, the DSO can even adjust the load to follow the expected supply of the system. An implementation example is given in Section 3 to complement the conceptual schematic.

## 3. Experimental case study

This section outlines the hardware and ICT infrastructures critical to our study. We detail the components and assumptions in supporting the experimental study and integration into existing systems.

### 3.1. Hardware specification

All assets, except the EV, were real components in the experiment. The EV with bidirectional charging was simulated with an identical model for both the emulator and the controller. This assumes perfect modeling of the EV battery and charging/discharging process. Physical components are from the NEST demonstrator at Empa in Switzerland (Richner, Heer, Largo, Marchesi, & Zimmermann, 2018), as Fig. 4 shows. The hardware was distributed around the research infrastructure. The time-stamped measurements allowed emulating the actual operation of a prosumer equipped with all the aforementioned assets. The total power of the emulated building combined all power measurements and the simulated EV power.

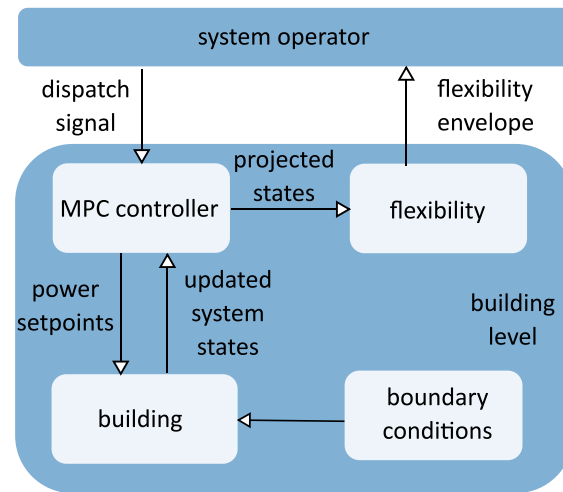


Fig. 3. Illustration of the information flow among the building, the controller and the system operator. At each time step, updated building state measurements are retrieved by the controller to solve the emission-aware OCP. The resultant state trajectories are used to quantify the flexibility envelope, which is self-reported to the DSO. Upon receipt, the DSO may request the prosumer to provide flexibility depending on the condition of the network.

The SH and DHW under control came from the residential unit marked with a red box in Fig. 4. The UMAR unit is equipped with water-based ceiling panels for space heating. The room temperature comfort zone of the whole unit was set as [22 °C, 23 °C]. The range was relaxed to [21 °C, 25 °C] during the daytime, specifically between 8 am and 8 pm, as occupants are likely absent during these hours. The comfort zone was defined on an ad hoc basis through feedback from occupants. Occupants can adjust the comfort zone without impacting the method's generality.

For domestic hot water heating, the tank's average temperature was maintained between [45 °C, 60 °C]. The lower limit was boosted to [59 °C, 60 °C] at least once a week to avoid Legionella contamination (Cai, You, Wang, Bindner, & Klyapovskiy, 2018). In our experiment, this timing was manually chosen to be Sunday morning between 4 am and 6 am. Additionally, a persistence forecast was used assuming that the future water draw will be the same as the day one week earlier. Preliminary studies employed a recurrent neural network and a Markov chains-based approach with one-year data. However, these did not enhance the forecast accuracy. This was due to the highly stochastic nature of human behavior at the household level and changes of occupants. Uncontrolled loads such as the cooking stove and the dishwasher were also located at the same unit. Therefore, consistent occupancy patterns for all the assets were ensured.

A Lithium-ion battery of 17.5 kWh with bi-directional charging/discharging power of  $\pm 5$  kW was operated.<sup>2</sup> Conversely, an EV of 50 kWh with bi-directional charging/discharging power of  $\pm 7$  kW was included as a simulated system component in the experiment. EV arrival and departure times were assumed to be known due to driver's input, which aligned with the large-scale field trial in Dudek (2021). PV electricity output was considered emission-free, but the power exported to the grid cannot offset the building's carbon footprint. The capacities of HPs for SH and DHW are 4 kW and 5.7 kW respectively. Additionally, COPs of 3.11 and 3.95 were identified from measurements and they were assumed to be constant in the OCP. Interested readers are referred to Cai (2020) for comprehensive description of test specifications and experiment plans.

### 3.2. Communication architecture

The interactions in the proposed system are illustrated in Fig. 5. Measurements were obtained from the Microsoft SQL database every

15 min (Empa, 2021). The forecast for ambient temperature and global solar irradiation was provided by the Federal Office of Meteorology and Climatology (MeteoSwiss) (Steppeler et al., 2003) every 12 h. Actuation setpoints were communicated through TwinCAT PLCs, which interacted with the hardware using ModBus or analog signals. The controller and PLCs were connected via an OPC server (Cai, 2020; OPC Foundation, 2022). The real-time forecast of electricity carbon intensity for Switzerland was provided by external sources (Swiss Federal Office of Energy, 2020), using data from the ENTSO-E Transparency Platform (ENTSO-E, 2021). Communication between the controller and the emulated DSO was achieved by exchanging csv files locally.

## 4. Results and analyses

This section details closed-loop control results, the controller's performance, and flexibility quantification and provision. In Sections 4.1 and 4.3, we present outcomes from physical experiments, whereas Section 4.2 discusses performance gain by comparing experimental results against simulated outcomes.

### 4.1. Closed-loop control results

The parameter identification problem formulated in Section 2.2 was solved using heuristic algorithms in Python by minimizing the non-convex nonlinear cost function presented in Eq. (29). The MPC controller solved the OCP from Section 2.3 every 15 min. The OCP was formulated with CVXPY (Diamond & Boyd, 2016) in Python 3 and solved using MOSEK (MOSEK, 2021). The control variables' optimal values were obtained over a 24 h horizon. Only the next time step's decision values were sent to the actuators via the Python-OPC UA client. Solution times per time step fell within  $20.75 \pm 16.05$  s. Large computation periods primarily resulted from the presence of integer variables, particularly when related constraints were active. However, these times were considered acceptable given the decision time interval of 15 min. All the hardware were equipped with dedicated meters, and all the measurements were stored in a Microsoft SQL database (Empa, 2021). Since the actuators cannot perfectly execute the set points, a distinction is made between the measured power and the power set point planned by the controller in the following results.

Model parameters were identified from 2019 data using the prediction error method (Lennart, 1999). The models were then re-sampled according to the set of inequidistant sampling time intervals shown in Fig. 1. During the experiment, we assumed the same power set point during each sampling time interval. The modeling accuracy of

<sup>2</sup> The onsite battery has a capacity of 96 kWh and we artificially limited its operating range to emulate a residential battery system.

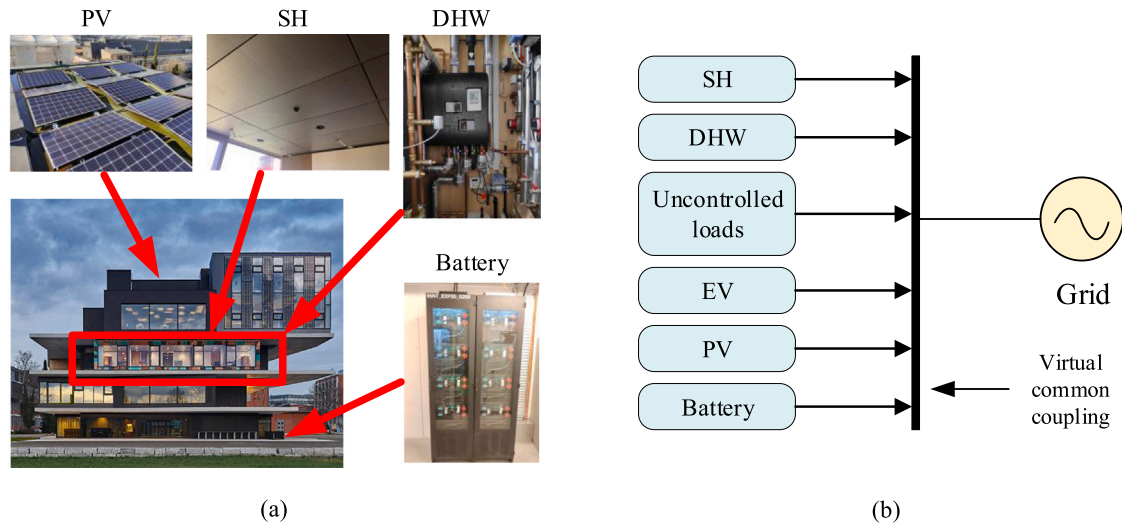


**Fig. 4.** Physical layer of the experimental setup (a) and its single-line representation (b). The physical layer shown in (a) includes SH with ceiling heating panels, DHW with a buffer tank, fixed loads of an apartment unit marked in the red box, a PV installation and a battery. The facility's thermal networks for SH and DHW were treated as fully separate for simplicity, despite being cascaded in reality. The PV installation is placed on the roof and the battery is located in the basement, which are not directly visible in the figure. The bi-directional charging EV is a simulated entity and is not visible here. All pictures are taken from [Empa \(2021\)](#). The spatially distributed hardware are virtually coupled via their timestamped measurements as shown in (b). Such a virtual coupling is seen as a billing point for the DSO. (For interpretation of the references to color in this figure legend, the reader is referred to the web version of this article.)

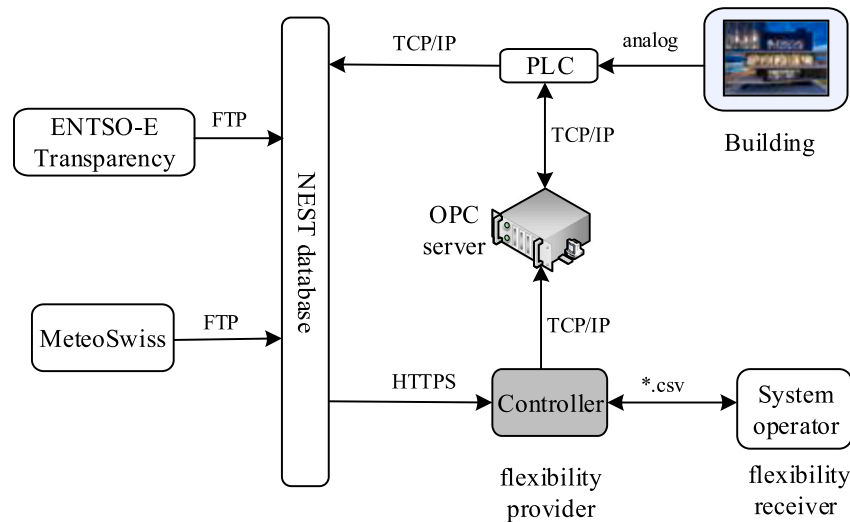


**Fig. 5.** Information exchange among the controller, the external information sources (e.g., MeteoSwiss), an emulated system operator and the hardware in the experiments.

each individual appliance is not presented here. However, additional experiments were carried out, where energy input for SH and DHW was minimized and their temperature were found to stay close to their lower limits ([Swiss Federal Office of Energy, 2020](#)). It is worth noting that this is a common experimental design for validating modeling accuracy, as demonstrated in [Bünning, Huber, Heer, Aboudonia, and Lygeros \(2020\)](#) and [Lian, Shi, Koch, and Jones \(2023\)](#). Additionally, the following experimental results further confirm modeling accuracy, as both SH and DHW temperatures stay within predefined limits while optimizing according to carbon intensity, except for dramatic disturbances.

In the week-long experiment, power set points of all controllable assets were obtained by solving the OCP formulated in Eq. (30) and the OCP with a modified objective function during flexibility provision. The rest of this section presents the controller decisions, realized power input and responses of all the assets, first detailing results for individual appliance. The net power exchange with the grid follows, as illustrated in [Fig. 9](#).

#### 4.1.1. Space heating

The temperatures of all three rooms are shown to approach their upper temperature limits in [Fig. 6\(a\)](#). This reflects the controller's strategy: maximizing electricity use when carbon intensity was low, and minimizing it when high. Significant temperature drops in Room 273 (marked by the gray periods ① – ⑤ in the figure) were due to extend window openings for hygiene, related to Covid. Excluding these instances, indoor temperature generally remained within the comfort zone.

Comparison between [Fig. 6\(b\)](#) and (c) indicates that actuators mostly follow the controller decisions even though there are mismatches. [Fig. 6\(d\)](#) shows that temperatures within Room 272 and Room 274 are mostly within the limits, whereas the accumulated temperature deviation reached around 4 Kh in Room 273 by the end of the experiment due to dramatic disturbances. We can also observe from [Fig. 6\(a\)](#) that indoor temperature occasionally exceeds the upper temperature limit such as the gray period ⑦. In general, such behavior

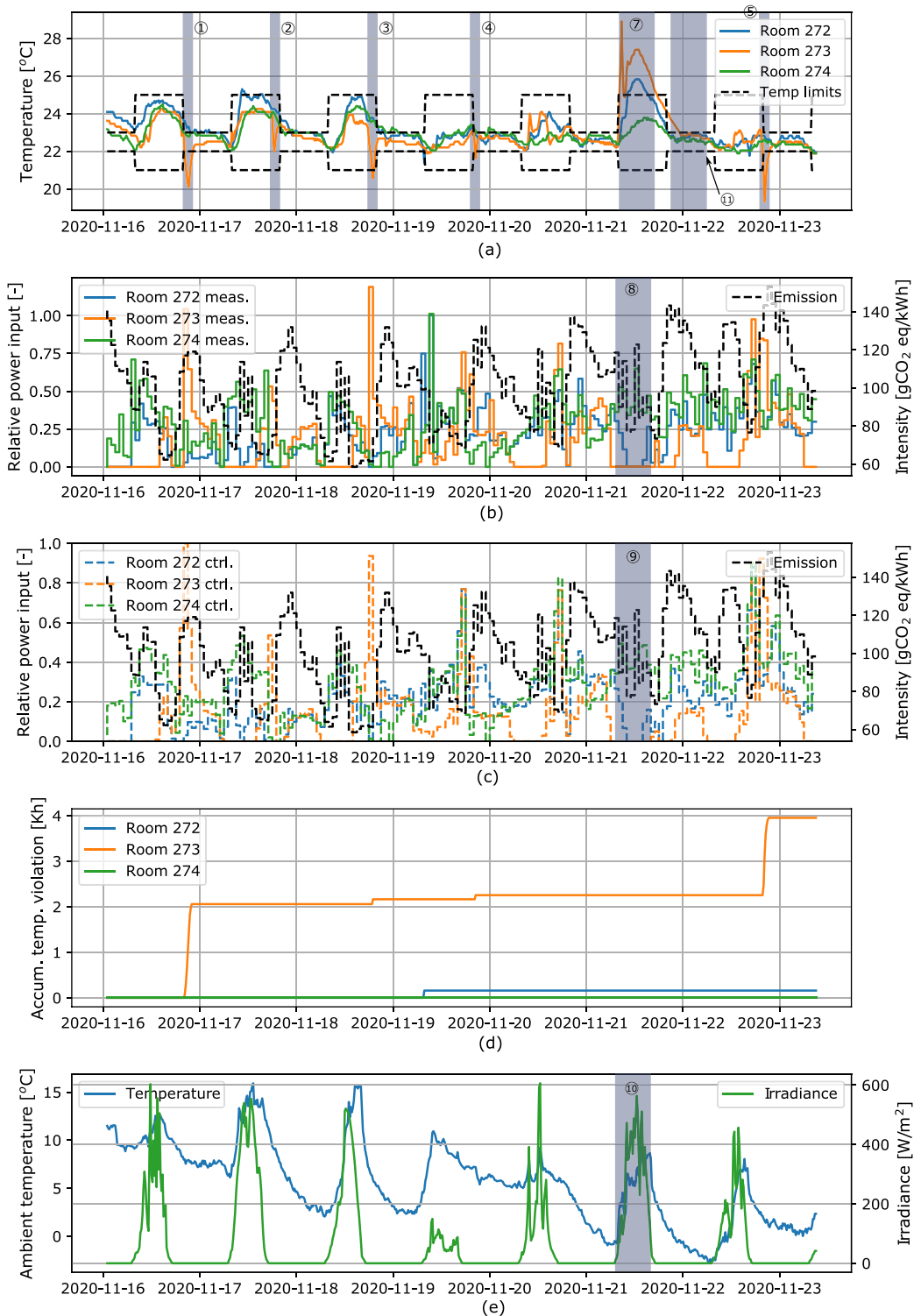


**Fig. 6.** Field experiment results of SH. (a) shows the measured temperatures of all three rooms. (b) shows the measured thermal power input into each room. (c) shows the thermal power input planned by the controller. The dashed black lines in (b) and (c) indicate the carbon-intensity profile. (d) shows the time-integral of room temperature deviations below the lower limit, measured in kelvin hours (Kh). (e) shows the ambient temperature and the irradiance measurements.

can be attributed to factors such as high solar irradiance, modeling errors, and internal gains that are not entirely captured. Notably, the solar irradiance as shown in the gray period ⑩ in Fig. 6(e) is not substantially higher than other days. Additionally, the measurements of the gray period ⑧ in Fig. 6(b) and the gray period ⑨ in Fig. 6(c) show that the controller decision and actual power input to Room 272

and Room 273 were close to 0 kW during the same period. Hence, the overshoot is more likely caused by dramatic internal gains.

#### 4.1.2. Domestic hot water

We can observe from Fig. 7(a) that the temperature is always within the predefined limits, indicating adequate hot water supply. Right before the boost of the lower temperature limit, energy is actively used



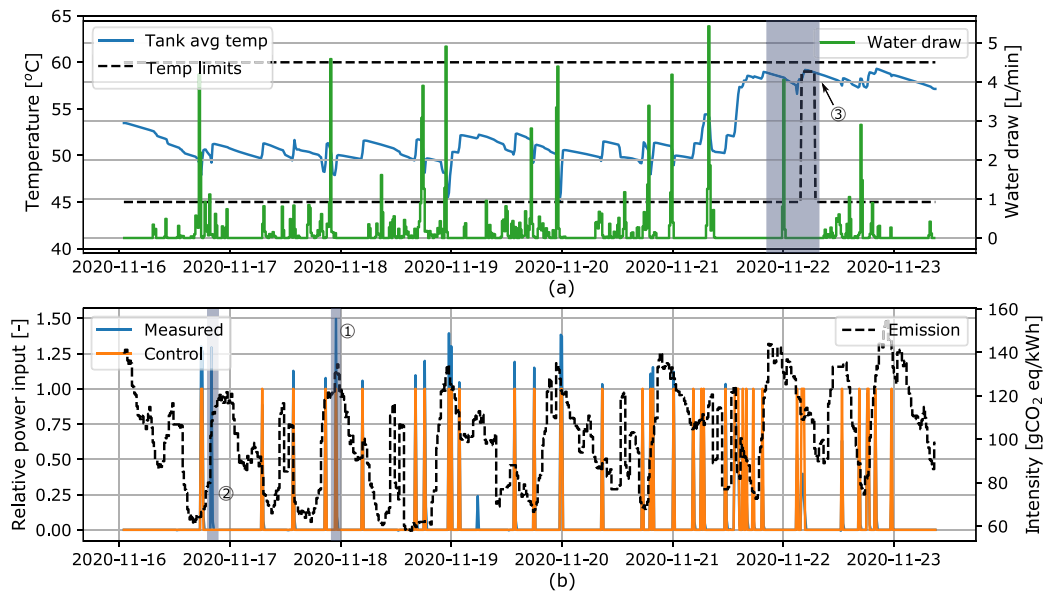


Fig. 7. Field experiment results of DHW. (a) shows the average tank temperature and the water draw over time. The planned and realized thermal power input into the tank are summarized in (b), in which the thermal power is normalized with a thermal power capacity inferred from historical data.

during the low carbon intensity period. However, Fig. 7(b) reveals that power consumption does not always inversely correlate with carbon intensity. For instance, unexpected high-energy demands, possibly from substantial water usage, caused power surges during peak carbon intensity periods (marked by the gray period ① in Fig. 7). Additionally, the net power exchange with the grid shown in Fig. 9 does not show a peak at this time (marked by the gray period ① in Fig. 9), implying that the power was supplied internally. We can also observe that the measured power input mostly follows control decisions, with exceptions such as that marked by the gray period ② in Fig. 7, which is a result of actuation errors. Additionally, thermal power inputs are dependent on the difference between tank temperature and inlet temperature. Hence, the measured power input varies over time.

#### 4.1.3. Other assets and grid interactions

For brevity, the results of all non-thermal loads are summarized in Fig. 8. Fig. 8(b) and (c) show the SOC and the charging/discharging power of the simulated EV.

The net electric power exchange with the grid aggregating all the assets is summarized in Fig. 9 alongside the electricity carbon intensity. Interestingly, the net power often inversely correlates with the carbon intensity profile. One notable grid export, during the gray period ②, can be traced back to an uncontrolled load profile's forecast error.

#### 4.2. Impact evaluation

To assess the controller's efficacy in reducing emissions, this work contrasts the presented results with a simulation on a virtual testbed. Although a simplified model is used in the closed-loop control, it is not accurate enough as a virtual testbed to emulate the physical system over one week. Hence, the digital twin developed in Khayatian, Bollinger, and Heer (2020), is used. This digital twin is calibrated using the data of entire 2019 at 1-min intervals with a CV-RMSE of 0.09, making it a suitable choice for the virtual experiment. Compared with other frequently used methods such as reference day, the proposed virtual experiment captures the high-resolution variation of carbon intensity profile.

The virtual experiment employs a hysteresis controller for both SH and DHW, representing industrial state-of-the-art. More specifically, the average water tank temperature limits are [55°C, 60°C] and the comfort zone of SH is the same as the physical experiment. DHW is

treated differently to ensure a sufficient temperature level to eliminate Legionella, which also replicates the existing industry practice. The EV is charged at full power right after being connected to the charger, and a hysteresis controller is applied afterward to ensure the minimum SOC level. Currently, there are no standard industrial practices as to design energy management systems covering all flexible devices. A self-consumption-oriented strategy is considered for the battery in addition to the hysteresis controllers mentioned above. It stores all PV production; for the rest of the time, it only discharges to cover the demand of other appliances. Note that the same carbon intensity profile is used in both the control and the impact evaluation. This assumes a perfect carbon intensity forecast. Interested readers are referred to Swiss Federal Office of Energy (2020) for the forecast accuracy.

We can observe that the total emission and the average carbon footprint of the consumed electricity are reduced by 12.5% and 16.5%, respectively. The reduction is realized by avoiding electricity imports during high carbon intensity periods. An example is marked by the gray period ① in Figs. 7 and 10. The reduction is not pronounced, which indicates that the benchmark control strategy mentioned above already reduce carbon footprint by promoting self-consumption.

#### 4.3. Flexibility quantification and provision

An example of online flexibility envelope quantification is provided in Fig. 11, which shows that flexibility potential considerably vary within the 24 h horizon. Results of the flexibility provision with an emulated DSO are in Fig. 12. We consider a scenario in which the DSO experiences network congestion due to low ambient temperature. More specifically, load peaks may be exacerbated due to simultaneous consumption from newly adopted HPs, which the distribution system may not be planned for. Thus, additional flexibility from buildings is needed to mitigate the issue. As per industry practice, ripple control (Westermann & John, 2007) has been used for decades for direct load control by broadcasting audio frequency signals to cease operation of devices such as HPs within a target group. However, ripple control represents unidirectional communication and addresses limited types of flexible devices. In the rest of this section, we demonstrate the proposed framework with an emulated DSO. More importantly, we show similar performance, namely keeping total power exchange with the grid close to 0 kW, can be achieved from the perspective of the DSO, while comfort levels and preferences of end users are shown to be respected.

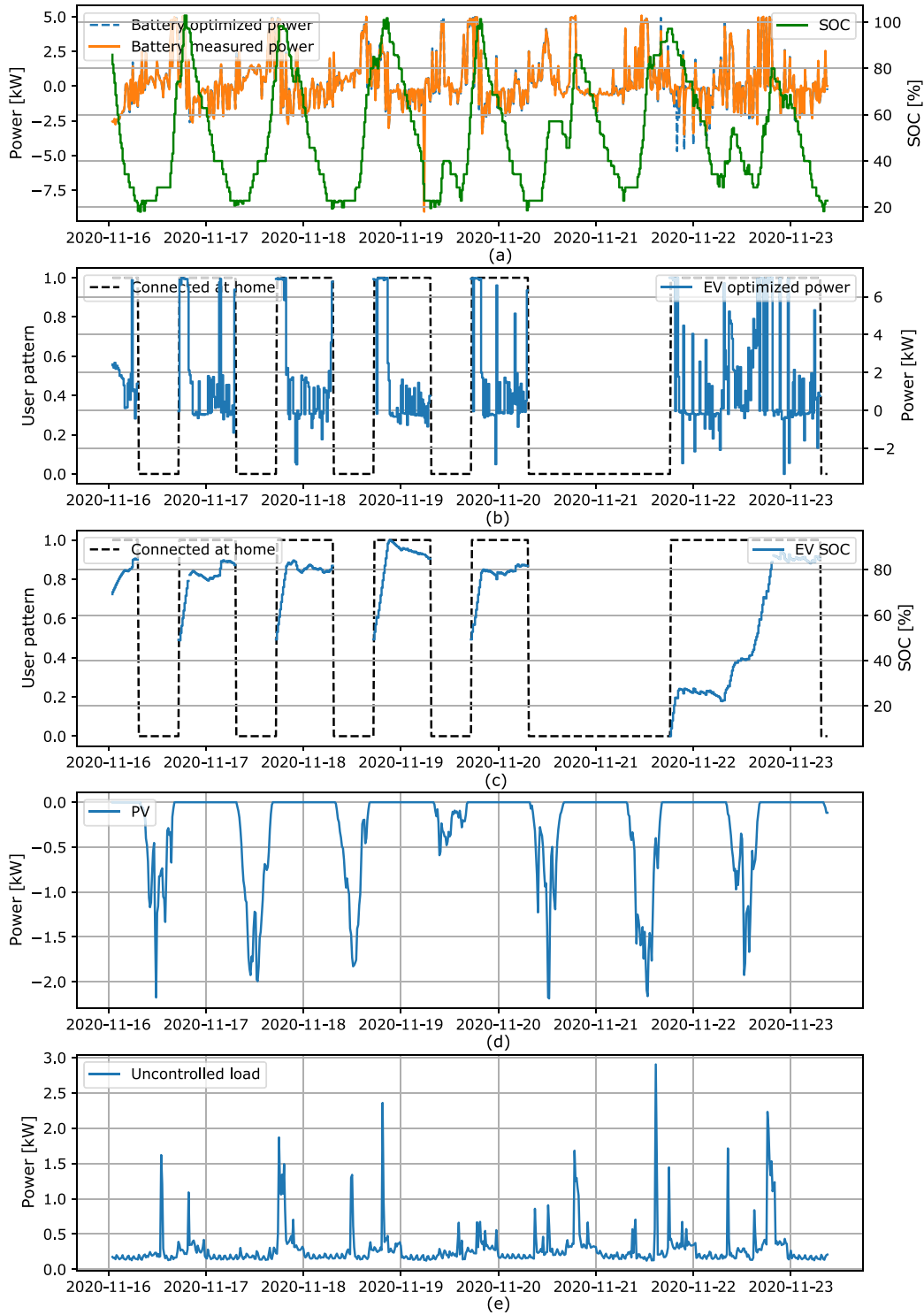


**Fig. 8.** Field experiment results of all non-thermal assets. (a) shows the battery's SOC, planned/measured charging/discharging power. (b) shows the simulated EV's charging/discharging power. (c) shows the EV's SOC. The dashed black line indicates the user's driving pattern, with 1 indicating that the EV is connected to the charger at home and 0 indicating the opposite. (d) and (e) show the measured PV power and the uncontrolled load respectively.

In the experiment, a building self-reports its flexibility envelope to the DSO, who in turn remains idle until flexibility needs are foreseen according to the weather forecast. The DSO examines the reported flexibility envelope shown in Fig. 11 and notifies flexibility provision to the building via  $(\tau_s, \tau_e, P) := (2020-11-21\ 21:00:00+01:00, 2020-11-22\ 06:30:00+01:00, 0\text{ kW})$  at the time marked by the vertical line ① in Fig. 12. Importantly,  $(\tau_s, \tau_e, P)$  needs to match the self-reported flexibility envelope (marked by the red box in Fig. 11). Within the

flexibility provision period (marked by the period between vertical lines ② and ③), the building tracks the set point. The results show that the total power exchange with the grid is reduced to a marginal level, although not strictly zero. This can be attributed to the actuation errors as observed in, Figs. 7 and 8. Besides, we can observe that the energy states of all devices are comfortably away from their lower limits (as seen at the end of the gray area ⑪ in the first plot of Fig. 6, and the end of the gray area ③ in the first plot of Fig. 7). This indicates

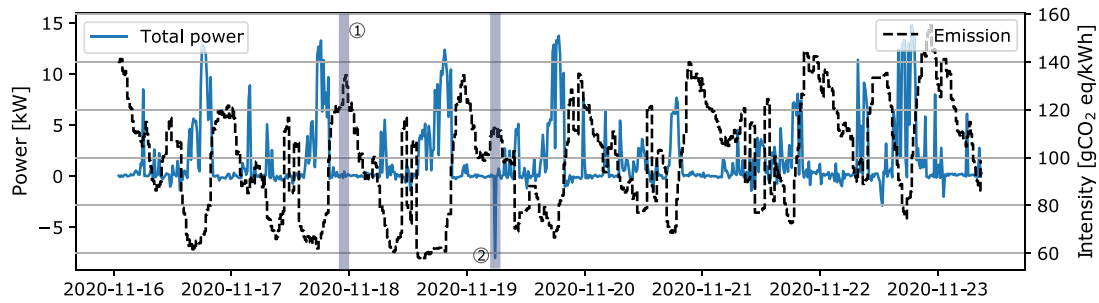


Fig. 9. Field experiment results of the net power exchange with the grid. The time series of the net electric power exchange is obtained by summing all respective power measurements and adding the simulated EV charging/discharging power.

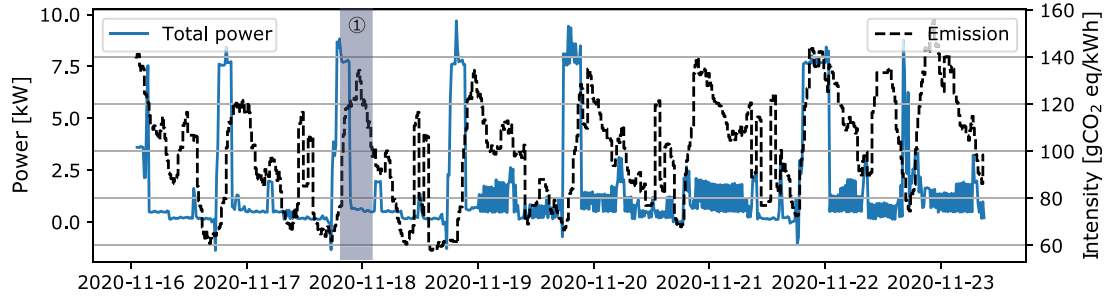


Fig. 10. Simulated results of the net power exchange with the grid.

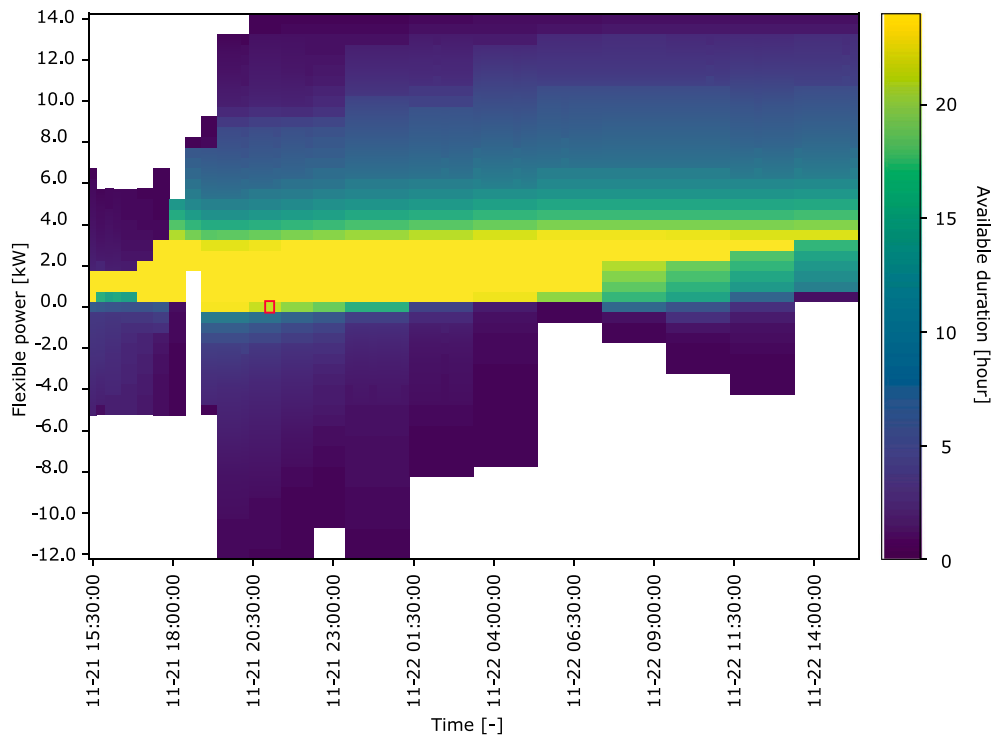
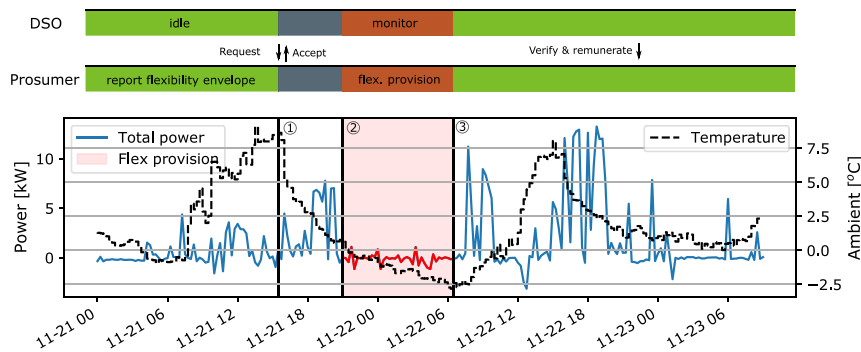


Fig. 11. An example of flexibility envelope exported by the controller.

that there are no immediate needs for electricity imports from the grid. Therefore, there is no risk of rebound effects. While the building activates its flexibility, the DSO continuously monitors the building and remunerates the service provider afterwards. A full discussion of the remuneration scheme lies beyond the scope of this study, but this remains an important issue for future research.

## 5. Discussion

Overall, the presented results demonstrate that the controller operates with emission-aware MPC as base strategy and can deviate from the optimal trajectory to provide flexibility upon request. In the experiments, control-oriented models, which were extracted from historical data, yielded satisfactory results both in terms of emission



**Fig. 12.** Results of flexibility provision example. The bars on top of the figure denotes the actions between the emulated DSO and the prosumer. The blue and red curves denote the aggregate power of all flexibility resources outside and inside flexibility provision period respectively. (For interpretation of the references to color in this figure legend, the reader is referred to the web version of this article.)

reduction and maintaining thermal comfort. This might be attributed to the unit being heated with water-based ceiling panels, which have slower dynamics than forced air heating (Bacher & Madsen, 2011). Additionally, the temperature was controlled within a small range.

Apart from the quantitative data, qualitative feedback on thermal comfort was also collected via an online feedback form during the experiments (Cai, 2020). For DHW, all feedback indicated “very satisfied”. As for the bedrooms, 37.5% of the time, the occupants indicated slightly cool indoor temperature in the 7-scale rating (cold, cool, slightly cool, neutral, slightly warm, warm, hot) matching low comfort violations. At other times, occupants expressed neutral opinions about the indoor temperature. We observed fatigue among users responding to survey requests, limiting the current survey. This suggests that the feedback strategy in the future needs to take a different form, especially for real-time control. Since the bi-directional EV was emulated, no feedback was gathered. Additionally, alternatives to the current definition of comfort zones and user preferences are available, such as continuous monitoring of occupancy coupled with real-time inference and forecasting. These alternatives have distinct cost and scalability implications compared to those discussed in our study.

Several challenges hinder scalability. Enhancing our methodology with advanced data-driven algorithms would facilitate its scalable application. Moreover, the varied levels of digitalization across regions necessitate modifications to adapt to controllable resources and achieve a balanced trade-off between costs and benefits. To the best of our knowledge, functional carbon credit systems at the building level are absent, and existing policies for energy transition primarily focus on cost. Regulatory changes are necessary for the adoption of the presented solution. Moreover, standardizing carbon footprint calculations and auditing procedures for emission reduction will provide necessary transparency and is critical for such regulations.

Moreover, reliability might be a concern. This is because reliability decreases as the element count increases in any series system. The proposed prosumer is an example of such series systems. Additionally, ripple control is implemented in an open-loop fashion and the response can be expected within 7 s (Westermann & John, 2007), whereas the proposed framework would take longer to quantify flexibility envelope and establish flexibility provision agreements. Moreover, communicating the flexibility envelope requires significant bandwidth, necessitating further simplification. All in all, the existing ripple control scheme excels in simplicity and responsiveness. In contrast, the presented framework is favorable for DSOs that require automation and an optimization-based approach due to the complexity of handling numerous resources. Taking these into account, future research might benefit from exploring a hybrid strategy that achieves a trade-off between performance and robustness. Although such assessment carries substantial policy implications, it remains underexplored in the existing literature.

## 6. Conclusion

Despite buildings’ promising active role in supporting the energy transition, challenges arise due to the involvement of diverse operational objectives and stakeholders. This work addresses gaps in experimental insights, focusing on emission-aware operations, flexibility quantification, and provision to DSO, alongside analyzing the impacts on and from occupants.

A week-long experiment demonstrates a 12.5% reduction in equivalent emissions compared to a benchmark controller that focused on maximizing PV self-consumption, while also indicating improvements in end users’ thermal comfort levels. The proposed flexibility provision framework, tested with an emulated distribution system operator, showcases a scenario where flexibility is utilized to mitigate network congestion, effectively coordinating behind-the-meter resources, maintaining user comfort and preferences under different conditions without rebound effects.

Nonetheless, limitations include not accounting for uncertainties in forecasts and model errors in the optimization problem. Additionally, challenges may arise if the maximum duration of flexibility provision is requested or when a DSO requires flexibility with a different lead time. It remains to be assessed whether flexibility can be reliably provided and comfort guaranteed. Future research directions include assessing more scenarios for robust flexibility quantification and exploring probabilistic flexibility representations to better manage uncertainties.

## CRedit authorship contribution statement

**Hanmin Cai:** Writing – review & editing, Writing – original draft, Visualization, Validation, Software, Methodology, Investigation, Formal analysis, Data curation, Conceptualization. **Philipp Heer:** Investigation, Formal analysis, Conceptualization, Methodology, Validation, Writing – original draft, Writing – review & editing.

## Declaration of competing interest

The authors declare that they have no known competing financial interests or personal relationships that could have appeared to influence the work reported in this paper.

## Data availability

Data will be made available on request.

## Acknowledgments

The project was funded by the Swiss Federal Office of Energy (Section: Energy Research and Cleantech) under the project SI/501841 “aliunid - Versorgung ‘neu’: Feldtest 1.1.2019–30.6.2020” and the Sustainable Demand Side Management for the Operation of Buildings (S-DSM) project under the contract number SI/502165-01. We would like to thank Reto Fricker, Sascha Stoller and Benjamin Huber for their support, and Fazel Khayatian for providing the digital twin of UMAR. We would also like to thank Charalampos Ziras, Julie Rousseau and Natasa Vulic for discussions and proofreading the draft. Finally, we acknowledge the members of IEA EBC Annex 82 for comments and suggestions.

## References

- Ahmed, R., Sreeram, V., Mishra, Y., & Arif, M. (2020). A review and evaluation of the state-of-the-art in PV solar power forecasting: Techniques and optimization. *Renewable and Sustainable Energy Reviews*, 124, Article 109792.
- Azizi, E., Ahmadihangar, R., Rosin, A., & Bolouki, S. (2022). Characterizing energy flexibility of buildings with electric vehicles and shiftable appliances on single building level and aggregated level. *Sustainable Cities and Society*, 84, Article 103999.
- Bacher, P., & Madsen, H. (2011). Identifying suitable models for the heat dynamics of buildings. *Energy and Buildings*, 43(7), 1511–1522.
- Bolzoni, A., Parisio, A., Todd, R., & Forsyth, A. (2021). Model predictive control for optimizing the flexibility of sustainable energy assets: An experimental case study. *International Journal of Electrical Power & Energy Systems*, 129, Article 106822.
- Bünning, F., Huber, B., Heer, P., Aboudonia, A., & Lygeros, J. (2020). Experimental demonstration of data predictive control for energy optimization and thermal comfort in buildings. *Energy and Buildings*, 211, Article 109792.
- Cai, H. (2020). Test specifications and experiment plans. <https://github.com/hacai44/GRIP/blob/main/Test%20specifications%20and%20experiment%20plans.pdf>. (Accessed 17 June 2021).
- Cai, H., You, S., Wang, J., Bindner, H. W., & Klyapovskiy, S. (2018). Technical assessment of electric heat boosters in low-temperature district heating based on combined heat and power analysis. *Energy*, 150, 938–949.
- De Coninck, R., & Helsén, L. (2016). Quantification of flexibility in buildings by cost curves—Methodology and application. *Applied Energy*, 162, 653–665.
- Decoussemaeker, A. (2020). *Model predictive control for energy optimization in an occupied apartment* (Ph.D. thesis), ETHz.
- Diamond, S., & Boyd, S. (2016). CVXPY: A python-embedded modeling language for convex optimization. *Journal of Machine Learning Research*, 17(83), 1–5.
- Dudek, E. (2021). The flexibility of domestic electric vehicle charging: The electric nation project. *IEEE Power and Energy Magazine*, 19(4), 16–27.
- Empa (2021). NEST wiki. <https://wiki.nestcloud.ch/wikipedia/>. (Accessed 14 April 2021).
- ENTSO-E (2021). ENTSO-E transparency platform. <https://transparency.entsoe.eu/>.
- Gasser, J., Cai, H., Karagiannopoulos, S., Heer, P., & Hug, G. (2021). Predictive energy management of residential buildings while self-reporting flexibility envelope. *Applied Energy*, 288, Article 116653.
- Global Alliance for Buildings and Construction, & International Energy Agency and United Nations Environment Programme (2020). 2020 Global status report for buildings and construction: Towards a zero-emission, efficient and resilient buildings and construction sector.
- Gupta, R., Pena-Bello, A., Streicher, K. N., Roduner, C., Farhat, Y., Thöni, D., et al. (2021). Spatial analysis of distribution grid capacity and costs to enable massive deployment of PV, electric mobility and electric heating. *Applied Energy*, 287, Article 116504.
- Heinrich, C., Ziras, C., Syri, A. L. A., & Bindner, H. W. (2020). EcoGrid 2.0: A large-scale field trial of a local flexibility market. *Applied Energy*, 261, Article 114399.
- Jensen, S. Ø., Marszał-Pomianowska, A., Lollini, R., Pasut, W., Knotzer, A., Engelmann, P., et al. (2017). IEA EBC annex 67 energy flexible buildings. *Energy and Buildings*, 155, 25–34.
- Khayatian, F., Bollinger, A., & Heer, P. (2020). Temporal resolution of measurements and the effects on calibrating building energy models. *arXiv preprint arXiv:2011.08974*.
- Le Dréau, J., Lopes, R. A., O’Connell, S., Finn, D., Hu, M., Queiroz, H., et al. (2023). Developing energy flexibility in clusters of buildings: A critical analysis of barriers from planning to operation. *Energy and Buildings*, Article 113608.
- Lennart, L. (1999). *System identification: theory for the user: vol. 28*, Upper Saddle River, NJ: PTR Prentice Hall.
- Li, R., Satchwell, A. J., Finn, D., Christensen, T. H., Kummert, M., Le Dréau, J., et al. (2022). Ten questions concerning energy flexibility in buildings. *Building and Environment*, 223, Article 109461.
- Li, H., Wang, Z., Hong, T., & Piette, M. A. (2021). Energy flexibility of residential buildings: A systematic review of characterization and quantification methods and applications. *Advances in Applied Energy*, Article 100054.
- Lian, Y., Shi, J., Koch, M., & Jones, C. N. (2023). Adaptive robust data-driven building control via bilevel reformulation: An experimental result. *IEEE Transactions on Control Systems Technology*, 31(6), 2420–2436.
- Ljung, L. (1998). System identification. In *Signal analysis and prediction* (pp. 163–173). Springer.
- Maasoumy, M., Rosenberg, C., Sangiovanni-Vincentelli, A., & Callaway, D. S. (2014). Model predictive control approach to online computation of demand-side flexibility of commercial buildings hvac systems for supply following. In *American control conference* (pp. 1082–1089).
- MOSEK (2021). Mosek APS. <https://www.mosek.com/>.
- Munankarmi, P., Jin, X., Ding, F., & Zhao, C. (2020). Quantification of load flexibility in residential buildings using home energy management systems. In *American control conference* (pp. 1311–1316).
- Nagy, Z., Gunay, B., Miller, C., Hahn, J., Ouf, M. M., Lee, S., et al. (2023). Ten questions concerning occupant-centric control and operations. *Building and Environment*, 242, Article 110518.
- OPC Foundation (2022). Unified architecture. <https://opcfoundation.org/about/opc-technologies/opc-ua/>.
- Ostergaard, J., Ziras, C., Bindner, H. W., Kazempour, J., Marinelli, M., Markussen, P., et al. (2021). Energy security through demand-side flexibility: The case of Denmark. *IEEE Power and Energy Magazine*, 19(2), 46–55.
- Péan, T., Costa-Castelló, R., & Salom, J. (2019). Price and carbon-based energy flexibility of residential heating and cooling loads using model predictive control. *Sustainable Cities and Society*, 50, Article 101579.
- Pergantis, E. N., Al Theeb, N., Dhillon, P., Ore, J. P., Ziviani, D., Groll, E. A., et al. (2024). Field demonstration of predictive heating control for an all-electric house in a cold climate. *Applied Energy*, 360, Article 122820.
- Richner, P., Heer, P., Largo, R., Marchesi, E., & Zimmermann, M. (2018). NEST—una plataforma para acelerar la innovación en edificios. *Informes de la Construcción*, 69(548), 222.
- Steppeler, J., Doms, G., Schättler, U., Bitzer, H., Gassmann, A., Damrath, U., et al. (2003). Meso-gamma scale forecasts using the nonhydrostatic model LM. *Meteorology and Atmospheric Physics*, 82(1), 75–96.
- Swiss Federal Office of Energy (2020). aliunid - versorgung neu: Feldtest 1.1.2019 – 30.6.2020. <https://www.aramis.admin.ch/Beteiligte/?ProjectID=43459>. (Accessed 19 April 2021).
- Thorsteinsson, S., Kalae, A. A. S., Vogler-Finck, P., Stærnøse, H. L., Katic, I., & Bendtsen, J. D. (2023). Long-term experimental study of price responsive predictive control in a real occupied single-family house with heat pump. *Applied Energy*, 347, Article 121398.
- Vigna, I., Perneti, R., Pasut, W., & Lollini, R. (2018). New domain for promoting energy efficiency: Energy flexible building cluster. *Sustainable Cities and Society*, 38, 526–533.
- Westermann, D., & John, A. (2007). Demand matching wind power generation with wide-area measurement and demand-side management. *IEEE Transactions on Energy Conversion*, 22, 145–149.